HHS Public Access

Author manuscript

J Opt Soc Am A Opt Image Sci Vis. Author manuscript; available in PMC 2015 June 14.

Published in final edited form as:

J Opt Soc Am A Opt Image Sci Vis. 2014 March 1; 31(3): 569–579.

Visualization of retinal vascular structure and perfusion with a nonconfocal adaptive optics scanning light ophthalmoscope

Yusufu N. Sulai[1], **Drew Scoles**[2], **Zachary Harvey**[3], and **Alfredo Dubra**[3,4,5,*]

[1]The Institute of Optics, University of Rochester, Rochester, New York 14627, USA

[2]Department of Biomedical Engineering, University of Rochester, Rochester, New York 14627, USA

[3]Department of Ophthalmology, Medical College of Wisconsin, Milwaukee, Wisconsin 53226, USA

[4]Department of Biophysics, Medical College of Wisconsin, Milwaukee, Wisconsin 53226, USA

[5]Department of Biomedical Engineering, Marquette University, Milwaukee, Wisconsin 53233, USA

Abstract

Imaging of the retinal vascular structure and perfusion was explored by confocal illumination and nonconfocal detection in an adaptive optics scanning light ophthalmoscope (AOSLO), as an extension of the work by Chui *et al.* [Biomed. Opt. Express **3**, 2537 (2012)]. Five different detection schemes were evaluated at multiple retinal locations: circular mask, annular mask, circular mask with filament, knife-edge, and split-detector. Given the superior image contrast in the reflectance and perfusion maps, the split-detection method was further tested using pupil apodization, polarized detection, and four different wavelengths. None of these variations provided noticeable contrast improvement. The noninvasive visualization of capillary flow and structure provided by AOSLO split-detection shows great promise for studying ocular and systemic conditions that affect the retinal vasculature.

1. INTRODUCTION

The human retina is a complex tissue composed of highly metabolic neurons and support cells that require an efficient vascular network for adequate supply of oxygen and nutrients. The retinal vasculature is affected in a large number of systemic and ocular conditions including stroke [1], diabetes [2], age-related macular degeneration [3], macular telangiectasia [4], retinal vascular occlusions [5], and glaucoma [6]. The high prevalence and potential severity of vision loss due to these conditions makes monitoring the structure and perfusion of the retinal vasculature critical.

*Corresponding author: adubra@mcw.edu.

OCIS codes: (110.1080) Active or adaptive optics; (290.4210) Multiple scattering; (170.4460) Ophthalmic optics and devices; (170.4470) Ophthalmology.

The current clinical standard for visualization of ocular vasculature perfusion and leakage are fluorescein angiography (FA) [7] and indocyanine green (ICG) angiography [8]. These procedures require the injection of exogenous dyes into the blood stream followed by fluorescence imaging with ~488 nm (FA) or ~790 nm (ICG) excitation light. The invasive nature of the injection, potential toxicity of the dyes [9], concerns about light safety [10], and patient discomfort have led to the exploration of less invasive optical imaging techniques referred to as motion contrast [11–20]. In these imaging modalities, contrast is mathematically derived from temporal variations in the amplitude, frequency, or phase of light collected from the retina. The fundamental assumption underlying this rapidly growing field is that these temporal changes are caused by the motion of blood cells. The reliance of these methods on somewhat rapid motion limits their ability to reveal leakage and therefore make it unlikely that they will fully replace fluorescein and ICG angiography. Moreover, motion contrast techniques are by definition susceptible to image registration errors, as residual uncorrected eye motion in an image sequence would generate artifactual contrast. Motion contrast angiography could, however, provide a lower cost, faster, safer, and less invasive complement to dye angiography.

Motion contrast angiography has been demonstrated in many different forms including single point laser Doppler velocimetry [11,12], scanning laser Doppler flowmetry [13,14], laser speckle flowmetry [15], Doppler optical coherence tomography (OCT) [16], differential fundus photography [17], and phase variance OCT [18]. When combined with adaptive optics (AO), these techniques can reveal even the finest retinal capillaries [20–24] in a way similar to FA [25,26]. Nonangiography ophthalmic AO techniques have also resolved cellular structure in the vessel walls [27], as well as individual blood cells [20].

Resolving retinal vascular beds in close proximity to strongly backscattering layers such as the nerve fiber or photoreceptor layers can be challenging when using imaging modalities with no or poor-axial sectioning. Chui *et al.* [28] overcame this problem in the AO scanning light ophthalmoscope (AOSLO) by laterally offsetting the confocal detector. This arrangement, which was originally demonstrated by Webb *et al.* [29], allows direct visualization of the blood vessels and capillary walls, as well as perfusion, through motion contrast. Here, we extend the work of Chui *et al.* [28] by exploring four nonconfocal AOSLO detection schemes and seek to improve the contrast of both the structural and perfusion images [27]. In addition to varying the dimensions and geometry of the detection apertures, illumination pupil apodization, polarized detection, and four different illumination wavelengths were also evaluated.

2. METHODS

A. Human Subjects

Three male subjects (26–29 years old) with mild refractive error (−4.75 D for subject JC_0200, −1.6 D for subject AD_1025, and 0 D for subject JC_1246) and no known history of eye disease were recruited for this study, which was approved by the Institutional Review Board at the Medical College of Wisconsin. The nature and possible risks of the study were explained to the subjects, after which written consent was obtained. The pupil of the eye was dilated and cycloplegia was induced with topical application of one drop of phenylephrine

hydrochloride (2.5%) and one drop of tropicamide (1%). The subject's head was stabilized with the use of a bite bar attached to a three axis translation stage, which was used to align the AOSLO exit pupil with the entrance pupil of the subject's eye.

B. AOSLO Imaging

A previously described AOSLO [30] was modified to compare five different detection schemes. This was achieved by placing different spatial filters in the retinal conjugate plane in front of the light detector(s). The spatial filters used, shown in Fig. 1, were:

1. Centered circular apertures with 1, 6, or 16 Airy disk diameters (ADDs).
2. Annular apertures with 16 ADDs outer diameter and 1, 3, or 6 ADD inner diameter. This is a form of dark-field detection, which in Webb *et al.*'s work [29] is referred to as the "Tyndall or indirect view."
3. A circular aperture, 16 ADD in diameter with a centered opaque filament oriented near horizontally, which was 1, 3, or 6 ADD in width. This form of dark-field detection was recently used by Scoles *et al.* [31] to visualize the retinal pigment epithelium cell mosaic in the living human eye.
4. A knife-edge test implemented by blocking a portion of a 16 ADD circular mask and using a nearly horizontal opaque tape. The edge of the tape within the aperture blocked half of the aperture plus an additional 0.5, 1.5, or 3 ADD (see Fig. 1). These values correspond to the annular and filament inner diameters tested, with an additional half-plane blocked.
5. Split-detection [32] was implemented by collecting the light on the left and right side of a circular aperture 20 ADD in diameter and a central vertical obscuration 1 or 3 ADD wide, using two different detectors.

The spatial filters were compared by imaging two retinal locations in subject JC_0200 with 790 nm light. The two retinal locations were 0.6° temporal, 0.6° inferior, and 5° nasal, 5° inferior, relative to fixation. These locations were chosen because they correspond to the edge of the foveal avascular zone (FAZ), where there is no nerve fiber layer (NFL), and an area with a strong NFL backscattering signal (~40 μm NFL thickness), respectively.

Later, elementary pupil apodization and polarization tests were performed using split-detection in subject AD_1025 with 790 nm light. The illumination pupil was apodized using an annular mask with 3.0 and 7.5 mm inner and outer diameter at the pupil of the eye, respectively. This was done in an attempt to extend the depth of field [33,34].

Polarized detection was tested by illuminating the eye with linearly polarized light (~10:1) and by filtering the light exiting the eye with a linear polarizer. Images of retinal capillaries were acquired with the polarizer oriented for maximum throughput, and then at 45 and 90° relative to that orientation.

Finally, images were also acquired with three other wavelengths (560, 600, and 680 nm mean wavelength, 10 nm bandwidth) in subject JC_1246.

C. Light Exposure

Because AOSLO vascular images often contain few distinct features that facilitate accurate registration, simultaneous image sequences focused on the photoreceptor layer were recorded using an additional confocal imaging channel. When using 790 nm light for vascular imaging, 680 nm light was used to image the photoreceptor mosaic. Conversely, when imaging vasculature with 560, 600, or 680 nm light, 790 nm light was used to obtain a registration signal. Wavefront sensing was performed using 850 nm light in all experimental conditions.

The AOSLO light sources used were superluminescent diodes (SLD; Superlum, Co. Cork, Ireland) for 680, 790, and 850 nm light and a supercontinuum source (NKT Photonics, Birkerød, Denmark) for 560 and 600 nm light. The 790 and 850 nm SLDs were modulated and turned on only during the imaging portion of the scanning raster. This improved the AO correction by only measuring aberrations over the imaged field of view and minimized light exposure. The optical powers measured at the pupil of the eye during imaging were 80 μW at 560 or 600 nm, 120 μW at 680 nm, 54 μW at 790 nm, and 5 μW at 850 nm. For the pupil apodization experiment, the power at the eye of the 790 nm source was reduced by 16% to ~45 μW.

Photochemical light toxicity was minimized by acquiring images with 560 and 600 nm light on nonoverlapping retinal areas. With a 1.25° field of view and a frame rate of 17 Hz, the exposure was selected to be least five times below the ANSI Z136.1 maximum permissible exposure for all wavelength combinations [35,36].

D. Image Processing and Analysis

For the pair of simultaneously acquired images using the split-detector method (Ch.1 and 2 in Fig. 1), a third sequence (referred to as the split-detector sequence) was calculated as the image difference between the two detectors divided by their sum.

Image sequences with 300 frames were acquired for all experimental settings. Of those, the 200 frames with the highest normalized cross-correlation when compared against a manually selected reference frame were registered using strip-based registration custom software [37] after removing the sinusoidal warping induced by the resonant optical scanner. An average image from each registered sequence was then created to visualize the retinal vasculature structure. The same sequences were processed to create motion contrast images that revealed the vascular perfusion, in a similar fashion to that used by Chui *et al.* [23]. This was accomplished by calculating the standard deviation of each pixel across the registered image sequence. These motion contrast images will henceforth be referred to as perfusion maps. No additional filtering or processing was performed to the images presented in this work.

The intensity profiles of individual capillaries along a short segment for all detection schemes were plotted. Each cross-section curve was normalized to its intensity in a ~6 μm band 10 μm away from the capillary center. These arbitrary values were chosen to aid a coarse comparison of the different detection schemes.

3. RESULTS

A. Image-Plane Spatial Filter Comparison

Spatial filters are compared in subject JC_0200 at the corner of the FAZ in Figs. 2–4, with reflectance in Fig. 2 and perfusion maps in Fig. 3. Capillary cross sections boxed in Figs. 2 and 3 are shown in Fig. 4 to allow comparison of capillary reflectance and perfusion map contrast across modalities. Further comparisons at the more eccentric location in the same subject (5° nasal and inferior from fixation) are shown in Figs. 5 and 6.

1. Circular Apertures—The confocal images of the edge of the FAZ collected with a 1 Airy disk circular pinhole (top left panel of Fig. 2) had a strong reflectance signal along the capillary center line with dark adjacent areas. This reflection was not uniform along the vessel length, and the bright areas possibly corresponded to astrocyte end-feet, pericytes, and/or vascular endothelial cells [27]. As the aperture size increases (top row of Fig. 2), thereby effectively transitioning from confocal to bright-field imaging, the vascular walls become more apparent, the overall contrast is reduced, and the image background becomes more uniform (Figs. 2–4). Interestingly, the larger apertures caused the capillary reflectance profile to change from having a single peak (unipolar) to having one peak and one trough (bipolar) relative to the background.

In retinal locations with relatively thick NFL, such as that shown in Fig. 5, the strong reflectance signal from the NFL prevented the visualization of the microvasculature for all circular detector sizes. Also, the granular NFL appearance means that residual errors in image registration create larger granular artifacts in the perfusion maps that cover the entire image.

2. Centered Obscurations—When imaging with the annular apertures or circular apertures with filaments, only the inner diameters were varied while the outer diameter was maintained at 16 ADD. The reflectance images (second and third rows of Fig. 2) and vascular cross sections (same rows, Fig. 4) did not change noticeably with either type of detection aperture or inner obscuration size. As with the large circular apertures, the capillary profiles were typically (but not always) bipolar. The perfusion maps on the other hand (Fig. 3 and red dashed curves in Fig. 4), showed a clear reduction in contrast with increasing obscuration size.

The same observations can be made from the images at 5° inferior and nasal from fixation (second and third rows of Figs. 5 and 6). Notably, the larger obscurations resulted in a stronger attenuation of the NFL signal, thus revealing the capillary network that serves the NFL more clearly. The perfusion maps at this retinal eccentricity (Fig. 6) were comparable to that of the FAZ, showing a contrast reduction with increasing inner diameter. This suggests that the confocal signal, which is blocked with the central circular (annular aperture) or rectangular block (filament), contains a nonnegligible amount of flow information.

3. Knife-Edge—Similar to the annular and circular apertures with a filament, the reflectance images in Fig. 2 showed comparable capillary walls contrast regardless of the

position of the straight edge of the obscuration. There was, however, a contrast reduction in the perfusion maps with increasing aperture blockage, albeit smaller than that observed when using filaments or circular apertures.

At the more eccentric retinal location (Fig. 5), the blocking of the confocal signal attenuated the light from the NFL, revealing the microvasculature in both the reflectance and perfusion maps. Of note, is that the contrasts and/or sharpness of the cellular structures in the largest blood vessel walls increased with obscuration size. In this imaging modality, there was also a clear bipolar appearance of the vessel walls regardless of the vessel orientation.

4. Split-Detector—One of the most notable features of the split-detector images is that low spatial frequency background variations attenuate with increasing detector separation. These images show high bipolar capillary contrast and what appears to be a mosaic of cellular structures, although without well-defined edges that would permit cell counting. The corresponding perfusion maps show moderate contrast with very uniform and minimal background, which makes these images the most amenable to automated vasculature segmentation when compared to the other detection schemes discussed previously.

When imaging at the more eccentric retinal location (Fig. 5), the NFL signal in the split-detector images was virtually negligible. This was likely the result of blocking the confocal signal as well as taking the difference between the two halves of the image plane signals. As with the images from the edge of the FAZ, the perfusion maps derived from the split-detector image sequences had the least image registration artifacts because of the substantial reduction of the NFL signal. Furthermore, this technique also provides the strongest (bipolar) contrast of the cellular structures flowing within the blood vessels (Media 1 in Fig. 10) and forming the walls of the larger vessels (Fig. 5).

Given the superior contrast of vascular and perfusion maps of the split-detection, we selected this method for further refinement and investigated pupil apodization, polarization, and wavelength.

B. Split-Detector and Pupil Apodization

In an attempt to extend the depth of field of the split-detection without sacrificing transverse resolution, we elongated the illumination point spread function by placing an annular pupil in the illumination path [34,38]. The resulting images acquired in subject AD_1025 show that the apodization blurs split-detector images with a reduction in image contrast in both reflectance and perfusion maps (Fig. 7).

C. Split-Detector and Exit Polarization

Given the development of polarization sensitive ophthalmoscopes [39–41] that exploit the birefringence properties of the human eye [42–44], we explored the effect of polarized split-detection. This was accomplished by placing a linear polarizer in the pupil conjugate plane in front of the detector while illuminating the eye with linearly polarized light in subject AD_1025. The images acquired at the edge of the FAZ and at 5° inferior-nasal (see Fig. 8) appeared blurred and had reduced contrast with the linear polarizer in place. Both

degradations increased as the polarizer was rotated away from maximum transmission because of a reduction in the signal.

D. Split-Detector and Wavelength

Finally, split-detector vascular imaging using visible wavelengths was evaluated as a potential avenue to increase contrast. This was accomplished by comparing images collected with 560 and 600 nm light against images acquired with 680 nm light. The images acquired in subject JC_1246 (see Fig. 9) showed higher contrast for 680 nm light compared to 560 and 600 nm light, and there were no obvious differences between the two shorter wavelengths. Perfusion maps acquired with shorter wavelengths had a substantially noisier background, which makes the segmentation of capillaries more challenging.

4. DISCUSSION

The AOSLO images captured with circular apertures cover the whole axial sectioning range, from the most confocal detection possible (1 ADD) to, effectively, bright-field imaging (16 ADD). In this transition, the intensity cross section of capillaries changed from unipolar to bipolar, which suggests that two different contrast mechanisms are at play. This was unexpected because nothing in the anatomy or the detection scheme suggests a preferential side of the capillary structure. This result might suggest that rays of light impinging on the central region of the retinal conjugate plane (~1 ADD) in front of the detector create the unipolar vessel profiles, whereas the rays outside the confocal region provide the bipolar signal. This observation was consistent across all detection methods tested.

Larger circular apertures provided less contrast overall, but they allowed for the visualization of the vascular walls at the FAZ in reflectance with a more uniform background. The uniform background was beneficial in that it attenuated image registration artifacts in the perfusion maps. However, the poor visualization of blood vessels within the NFL with this technique means that a centered circular detection aperture is not optimal for vascular structure or perfusion outside the FAZ.

Of the tested conditions, the split-detection produced the highest contrast in structural (reflectance) and perfusion maps. Multiple scattering is the most likely source of contrast in all of the scanning ophthalmoscopes that block the confocal signal [28], including the four tested here, but a concrete mathematical description of these imaging modalities is still lacking. A possible explanation could be as follows: integrating the two-dimensional light intensity distribution along one direction in the pinhole plane of an AOSLO yields a one-dimensional (1D) function. Like all 1D functions, it can be decomposed as the sum of a symmetric and an anti-symmetric component. If this 1D intensity function, which corresponds to a single pixel in the image, is formed by the incoherent addition of photons, then annular masks and circular masks with or without filament will only provide information about the symmetric component of the intensity distribution at the aperture plane. Split-detection, as proposed here, is effectively the ratio of the anti-symmetric to the symmetric component of the intensity distribution, while the knife-edge is a combination of both. This means that the virtual elimination of the NFL signal in the split-detector images indicates that the NFL outside the central 1 ADD produces a mostly symmetric intensity

distribution in the image plane. Vasculature, however, can be seen in images acquired with all of the detection techniques, provided it is not overwhelmed by the NFL signal. This strongly suggests that retinal vasculature generates both symmetric and anti-symmetric intensity distributions at the detection plane. Because of the attenuation of the NFL signal with the split-detection method, this technique provides superior vessel wall contrast, as well as superior contrast of the perfusion maps, compared to the other detection techniques.

The disadvantage of such an asymmetric detection scheme is the perfusion maps of vessels oriented parallel to the split-detector edge (vertical, in this case) appear as two parallel lines outlining the perfused lumen, as illustrated in Fig. 10. Interestingly, the vertical portion of the capillary appears larger than the horizontal one in the perfusion map image. This should be further investigated before using this technique to quantify perfused lumen diameter. These artifacts could potentially be eliminated by dividing the nonconfocal signal using four quadrant detectors, and then generating an image that is a combination of horizontal and vertical split-detection.

One of the most striking features of split-detection is the high contrast of individual blood cells flowing through the retina capillaries, as seen in Media 1. Individual raw images also show the effect of the asymmetric detection with each blood cell appearing dark on the left and bright on the right, which strongly resemble images collected using differential phase microscopy techniques [45,46].

An additional benefit of split-detection is the contrast in the wall structures in the large vessels (white arrows in bottom right panel of Fig. 5). These structures correspond well with those reported by Chui *et al.* [27], and they are likely endothelial cells and/or pericytes.

Neither annular pupil apodization nor variations in the exit polarization seemed to enhance the contrast or SNR in split-detector images or their corresponding perfusion maps. This must be kept in mind when using instruments with polarizing elements in the imaging path.

The reasons for inferior contrast in reflectance and perfusion maps when using visible wavelengths are not trivial. For reasons that we do not fully understand but might relate to patient comfort, both AOSLO image (qualitative) sharpness and the wavefront sensor data indicates that the tear film breaks faster when using 560 and 600 nm light than when using 680 or 790 nm light. The tear film breakup affects the image sharpness both directly and indirectly through poor AO correction. We do not expect intraocular scattering to significantly degrade split-detector images because it should produce a relatively uniform background and most likely would create a symmetric intensity profile that would be removed with the subtraction of the signal from both detectors.

5. CONCLUSIONS

We have investigated the use of nonconfocal detection for imaging retinal vasculature in an AOSLO. The data indicates that among the five detection schemes investigated, the split-detector performs best in terms of revealing vessel and capillary walls with the most detail and contrast across all retinal locations and depths. Standard deviation maps derived from split-detector image sequences revealed perfusion with minimal background and repeatable

artifacts. These artifacts need to be better understood before reliable lumen diameter quantification can be achieved.

An elementary interpretation of the distribution of light on the retina conjugate plane was proposed to explain some of the findings across the different detection schemes evaluated here. The bipolar cross section of the capillary intensity profiles in the nonconfocal detection schemes remains unexplained, despite the absence of a preferential direction or side, as in the case of annular apertures.

The image plane nonconfocal split-detector method demonstrated here is similar to the differential amplitude method proposed by Wilson and Hamilton [32]. Other phase [47] and split-detector methods [46,48,49] have been proposed in microscopy and the encouraging results of this paper will hopefully inspire the translation of more microscopy techniques to ophthalmoscopy.

Despite our incomplete understanding of the source of contrast and appearance of the split-detector images, this technique shows great potential as a high-resolution noninvasive screening and monitoring tool for conditions that affect the retinal vasculature.

Acknowledgments

The authors would like to thank Robert F. Cooper and Benjamin Sajdak for their contributions to this work. Funding was provided by the Glaucoma Research Foundation Catalyst for a Cure initiative and NIH grants P30EY001931, UL1RR031973, and T32GM007356. Alfredo Dubra-Suarez is the recipient of a Career Development Award from Research to Prevent Blindness and a Career Award at the Scientific Interface from the Burroughs Wellcome Fund. This research was also supported by grants from the RD & Linda Peters Foundation and an unrestricted departmental grant from Research to Prevent Blindness. This investigation was conducted in a facility constructed with support from the Research Facilities Improvement Program; grant number C06-RR016511 from the National Center for Research Resources, NIH.

References

1. Patton N, Aslam T, MacGillivray T, Pattie A, Deary IJ, Dhillon B. Retinal vascular image analysis as a potential screening tool for cerebrovascular disease: a rationale based on homology between cerebral and retinal microvasculatures. J Anat. 2005; 206:319–348. [PubMed: 15817102]
2. Kohner EM, Hamilton AM, Saunders SJ, Sutcliffe BA, Bulpitt CJ. The retinal blood flow in diabetes. Diabetologia. 1975; 11:27–33. [PubMed: 1140516]
3. Kulkarni AD, Kuppermann BD. Wet age-related macular degeneration. Adv Drug Deliv Rev. 2005; 57:1994–2009. [PubMed: 16309781]
4. Gass JD, Oyakawa RT. Idiopathic juxtafoveolar retinal telangiectasis. Arch Ophthalmol. 1982; 100:769–780. [PubMed: 7082207]
5. Stern WH, Archer DB. Retinal vascular occlusion. Annu Rev Med. 1981; 32:101–106. [PubMed: 7013655]
6. Wolf S, Arend O, Sponsel WE, Schulte K, Cantor LB, Reim M. Retinal hemodynamics using scanning laser ophthalmoscopy and hemorheology in chronic open-angle glaucoma. Ophthalmology. 1993; 100:1561–1566. [PubMed: 8414416]
7. Ffytche TJ, Shilling JS, Chisholm IH, Federman JL. Indications for fluorescein angiography in disease of the ocular fundus: a review. J R Soc Med. 1980; 73:362–365. [PubMed: 7017129]
8. Stanga PE, Lim JI, Hamilton P. Indocyanine green angiography in chorioretinal diseases: indications and interpretation: an evidence-based update. Ophthalmology. 2003; 110:15–21. [PubMed: 12511340]

9. Chazan BI, Balodimos MC, Koncz L. Untoward effects of fluorescein retinal angiography in diabetic patients. Ann Ophthalmol. 1971; 3:42. [PubMed: 5163947]
10. Cideciyan AV, Jacobson SG, Aleman TS, Gu D, Pearce-Kelling SE, Sumaroka A, Acland GM, Aguirre GD. In vivo dynamics of retinal injury and repair in the rhodopsin mutant dog model of human retinitis pigmentosa. Proc Natl Acad Sci USA. 2005; 102:5233–5238. [PubMed: 15784735]
11. Tanaka T, Riva C, Ben-Sira I. Blood velocity measurements in human retinal vessels. Science. 1974; 186:830–831. [PubMed: 4469681]
12. Riva CE, Grunwald JE, Sinclair SH, Petrig BL. Blood velocity and volumetric flow rate in human retinal vessels. Investig Ophthalmol Vis Sci. 1985; 26:1124–1132. [PubMed: 4019103]
13. Wolf S, Arend O, Toonen H, Bertram B, Jung F, Reim M. Retinal capillary blood flow measurement with a scanning laser ophthalmoscope. Preliminary results. Ophthalmology. 1991; 98:996–1000. [PubMed: 1866155]
14. Michelson G, Schmauss B. Two dimensional mapping of the perfusion of the retina and optic nerve head. Br J Ophthalmol. 1995; 79:1126–1132. [PubMed: 8562550]
15. Tamaki Y, Araie M, Tomita K, Nagahara M, Tomidokoro A, Fujii H. Real-time measurement of human optic nerve head and choroid circulation, using the laser speckle phenomenon. Jpn J Ophthalmol. 1997; 41:49–54. [PubMed: 9147189]
16. Yazdanfar S, Rollins AM, Izatt JA. Imaging and velocimetry of the human retinal circulation with color Doppler optical coherence tomography. Opt Lett. 2000; 25:1448–1450. [PubMed: 18066244]
17. Nelson DA, Krupsky S, Pollack A, Aloni E, Belkin M, Vanzetta I, Rosner M, Grinvald A. Special report: noninvasive multi-parameter functional optical imaging of the eye. Ophthalmic Surg Lasers Imaging. 2005; 36:57–66. [PubMed: 15688972]
18. Fingler J, Zawadzki RJ, Werner JS, Schwartz D, Fraser SE. Volumetric microvascular imaging of human retina using optical coherence tomography with a novel motion contrast technique. Opt Express. 2009; 17:22190–22200. [PubMed: 19997465]
19. Tam J, Tiruveedhula P, Roorda A. Characterization of single-file flow through human retinal parafoveal capillaries using an adaptive optics scanning laser ophthalmoscope. Biomed Opt Express. 2011; 2:781–793. [PubMed: 21483603]
20. Bedggood P, Metha A. Direct visualization and characterization of erythrocyte flow in human retinal capillaries. Biomed Opt Express. 2012; 3:3264–3277. [PubMed: 23243576]
21. Tam J, Martin JA, Roorda A. Non-invasive visualization and analysis of parafoveal capillaries in humans. Investig Ophthamol Vis Sci. 2010; 51:1691–1698.
22. Dubis AM, Hansen BR, Cooper RF, Beringer J, Dubra A, Carroll J. Relationship between the foveal avascular zone and foveal pit morphology. Investig Ophthamol Vis Sci. 2012; 53:1628–1636.
23. Chui TYP, Zhong Z, Song H, Burns SA. Foveal avascular zone and its relationship to foveal pit shape. Optom Vis Sci. 2012; 89:602–661. [PubMed: 22426172]
24. Kurokawa K, Sasaki K, Makita S, Hong YJ, Yasuno Y. Three-dimensional retinal and choroidal capillary imaging by power Doppler optical coherence angiography with adaptive optics. Opt Express. 2012; 20:22796–22812. [PubMed: 23037430]
25. Scoles D, Gray DC, Hunter JJ, Wolfe R, Gee BP, Geng Y, Masella BD, Libby RT, Russell S, Williams DR, Merigan WH. In-vivo imaging of retinal nerve fiber layer vasculature: imaging histology comparison. BMC Ophthalmol. 2009; 9:9. [PubMed: 19698151]
26. Pinhas A, Dubow M, Shah N, Chui TYP, Scoles DH, Sulai YN, Weitz R, Walsh JB, Carroll J, Dubra A, Rosen RB. In vivo imaging of human retinal microvasculature using adaptive optics scanning light ophthalmoscope fluorescein angiography. Biomed Opt Express. 2013; 4:1305–1317. [PubMed: 24009994]
27. Chui TYP, Gast TJ, Burns SA. Imaging of vascular wall fine structure in the human retina using adaptive optics scanning laser ophthalmoscopy. Investig Ophthamol Vis Sci. 2013; 54:7115–7124.
28. Chui TYP, VanNasdale DA, Burns SA. The use of forward scatter to improve retinal vascular imaging with an adaptive optics scanning laser ophthalmoscope. Biomed Opt Express. 2012; 3:2537–2549. [PubMed: 23082294]

29. Webb RH, Hughes GW, Delori FC. Confocal scanning laser ophthalmoscope. Appl Opt. 1987; 26:1492–1499. [PubMed: 20454349]
30. Dubra A, Sulai Y. Reflective afocal broadband adaptive optics scanning ophthalmoscope. Biomed Opt Express. 2011; 2:1757–1768. [PubMed: 21698035]
31. Scoles D, Sulai YN, Dubra A. In vivo dark-field imaging of the retinal pigment epithelium cellmosaic. Biomed Opt Express. 2013; 4:1710–1723. [PubMed: 24049692]
32. Wilson T, Hamilton DK. Differential amplitude contrast imaging in the scanning optical microscope. Appl Phys B. 1983; 32:187–191.
33. Linfoot EH, Wolf E. Diffraction images in systems with an annular aperture. Proc Phys Soc B. 1953; 66:145.
34. Sulai YN, Dubra A. Adaptive optics scanning ophthalmoscopy with annular pupils. Biomed Opt Express. 2012; 3:1647–1661. [PubMed: 22808435]
35. ANSI Z136.1. American national standard for safe use of lasers. Laser Institute of America; 2007.
36. Delori FC, Webb RH, Sliney DH. Maximum permissible exposures for ocular safety (ANSI 2000), with emphasis on ophthalmic devices. J Opt Soc Am A. 2007; 24:1250–1265.
37. Dubra, A.; Harvey, Z. Registration of 2D images from fast scanning ophthalmic instruments. The 4th International Workshop on Biomedical Image Registration; Lübeck, Germany. 2010. p. 60-71.
38. Born, M.; Wolf, E. Principles of Optics. 6. Pergamon; 1980. (corrected) ed
39. Greenfield DS, Knighton RW, Huang XR. Effect of corneal polarization axis on assessment of retinal nerve fiber layer thickness by scanning laser polarimetry. Am J Ophthalmol. 2000; 129:715–722. [PubMed: 10926978]
40. Cense B, Chen TC, Park BH, Pierce MC, de Boer JF. Invivo depth-resolved birefringence measurements of the human retinal nerve fiber layer by polarization-sensitive optical coherence tomography. Opt Lett. 2002; 27:1610–1612. [PubMed: 18026517]
41. Cense B, Gao W, Brown JM, Jones SM, Jonnal RS, Mujat M, Park BH, de Boer JF, Miller DT. Retinal imaging with polarization-sensitive optical coherence tomography and adaptive optics. Opt Express. 2009; 17:21634–21651. [PubMed: 19997405]
42. Bour, LJ. Polarized light and the eye. In: Cronly-Dillon, JR., editor. Vision and Visual Dysfunction. MacMillan; 1991. p. 310-325.
43. Knighton RW, Huang XR. Linear birefringence of the central human cornea. Investig Ophthamol Vis Sci. 2002; 43:82–86.
44. Bueno JM, Campbell MCW. Polarization properties of the in vitro old human crystalline lens. Ophthalmic Physiolog Opt. 2003; 23:109–118.
45. Nomarski GJ. Microintérferomtrè différentiel à ondes polarisées. J Physiol Paris. 1955; 16:S9–S13.
46. Hamilton DK, Sheppard CJR. Differential phase-contrast in scanning optical microscopy. J Microsc. 1984; 133:27–39.
47. Ford TN, Chu KK, Mertz J. Phase-gradient microscopy in thick tissue with oblique back-illumination. Nat Methods. 2012; 9:1195–1197. [PubMed: 23103879]
48. Kawata Y, Juškaitis R, Tanaka T, Wilson T, Kawata S. Differential phase-contrast microscope with a split-detector for the readout system of a multilayered optical memory. Appl Opt. 1996; 35:2466–2470. [PubMed: 21085383]
49. Amos WB, Reichelt S, Cattermole DM, Laufer J. Re-evaluation of differential phase contrast (DPC) in a scanning laser microscope using a split-detector as an alternative to differential interference contrast (DIC) optics. J Microsc. 2003; 210:166–175. [PubMed: 12753099]

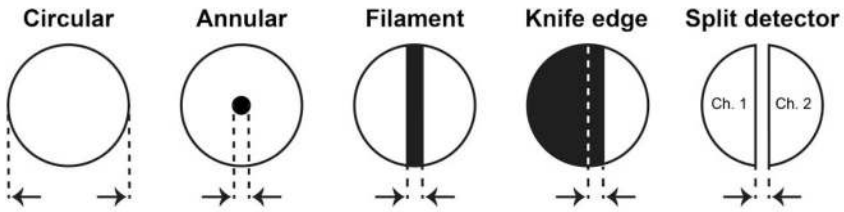

Fig. 1.

Masks placed in the retinal conjugate plane in front of the AOSLO point detector(s), with black denoting opaque regions. The arrows indicate the sizes referenced in the text. Split-detection is the only detection scheme with two detectors (Ch. 1 and 2).

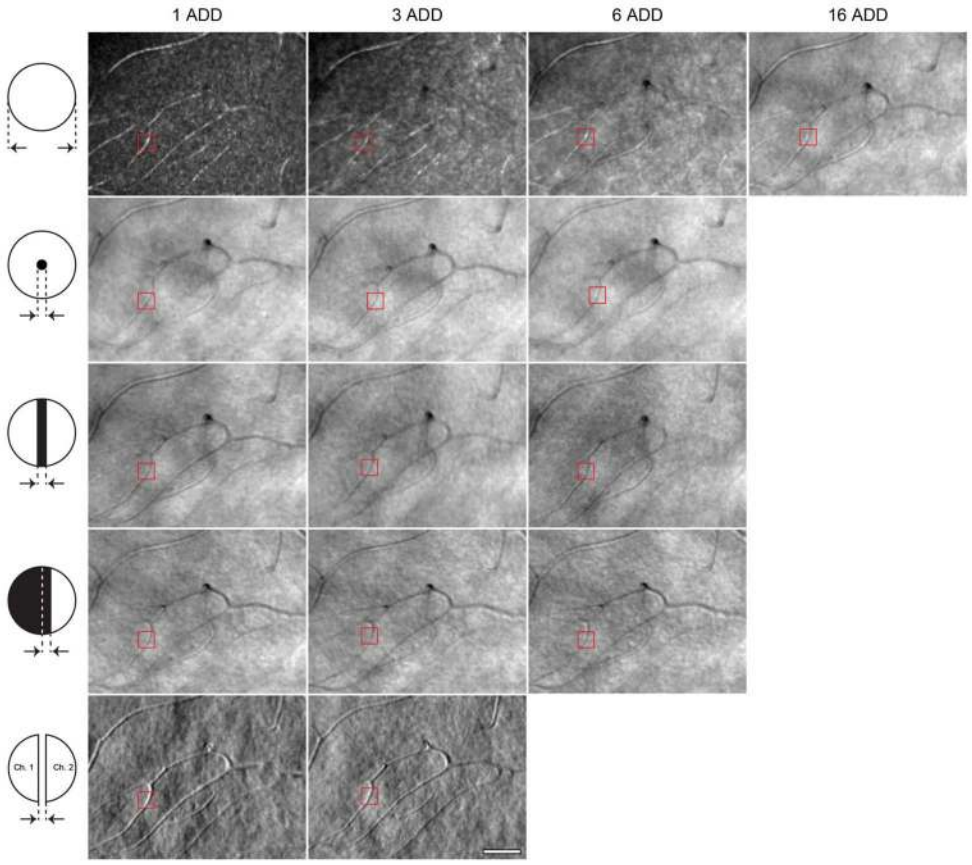

Fig. 2.

Reflectance AOSLO images of the inferior-temporal corner of the FAZ (0.6° temporal and inferior from fixation) collected in subject JC_0200 using the following detection apertures: circular, annulus, circular with an opaque filament, knife-edge, and split-detector. The red boxes indicate the vessel segment from which the intensity profiles in Fig. 4 are plotted. Scale bar is 50 μm across.

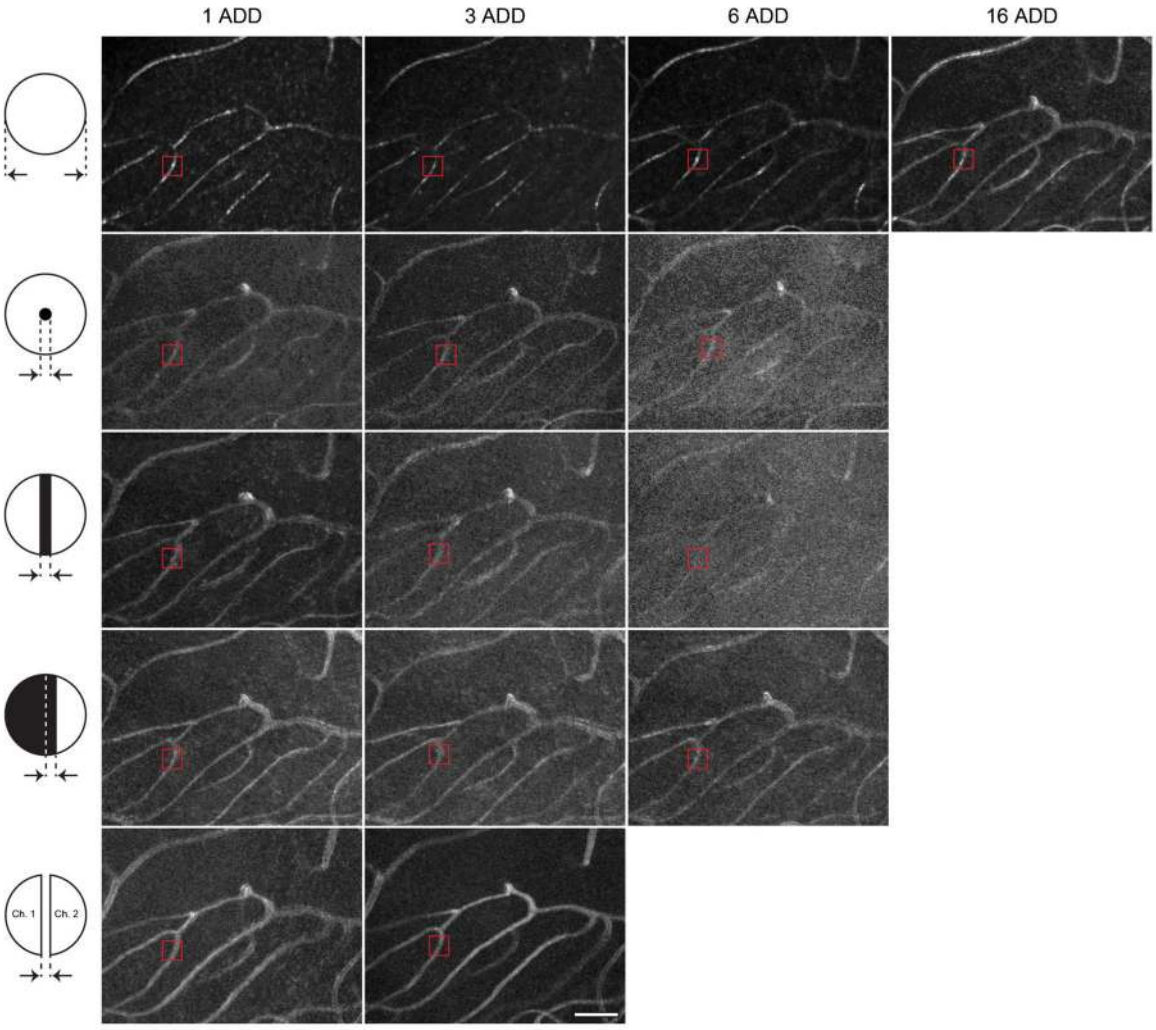

Fig. 3.

Perfusion maps corresponding to the image sequences averaged to create Fig. 2. The red boxes indicate the vessel segment from which the intensity profiles in Fig. 4 are plotted. Scale bar is 50 μm.

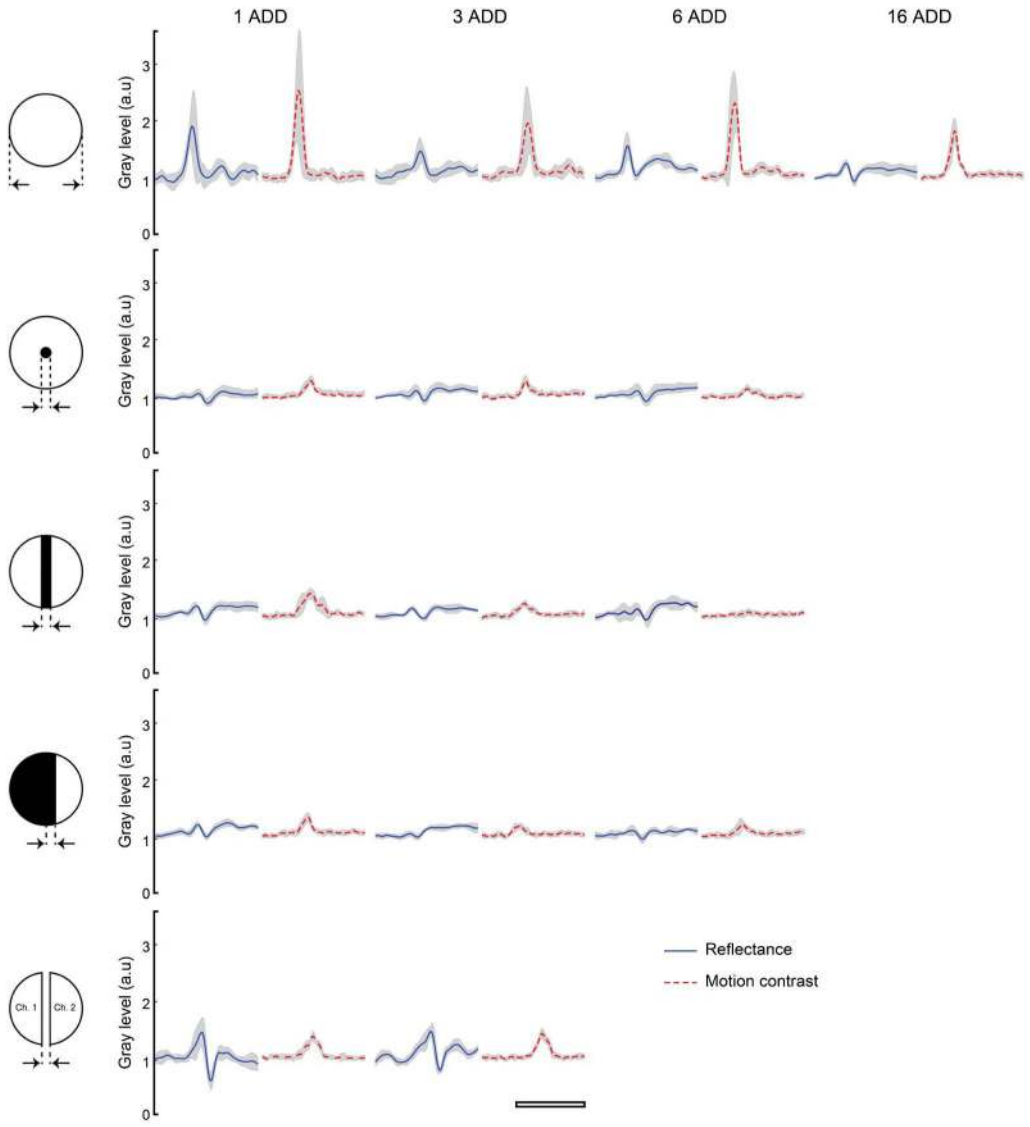

Fig. 4.

Intensity profiles of the vessel boxed in the reflectance images of Fig. 2 (blue, solid) and the perfusion maps of Fig. 3 (red, dashed). Each curve is normalized to its background (nonvessel values) and the shaded regions correspond to ±1 standard deviation away from the mean. The vertical axes refer to gray levels in arbitrary units. Scale bar is 20 μm across.

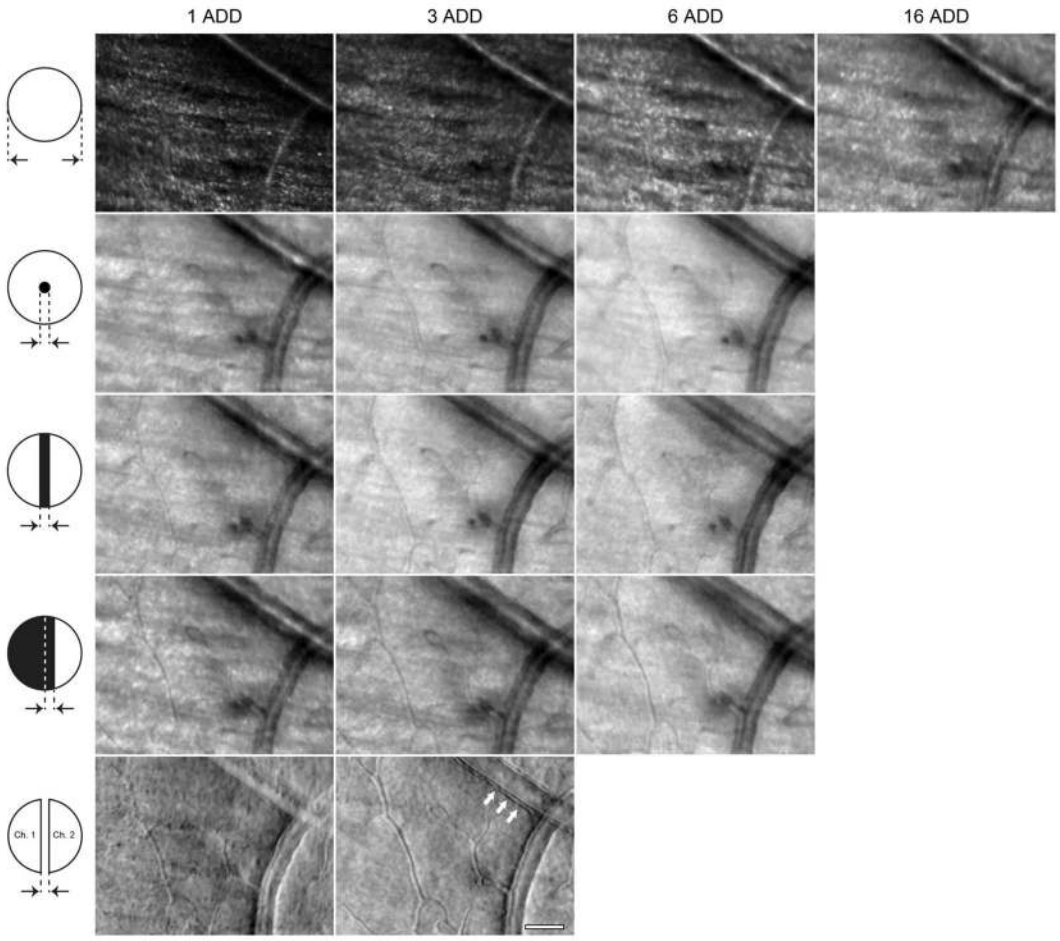

Fig. 5.

Reflectance AOSLO images at 5° nasal and inferior from fixation collected in subject JC_0200 using the following detection apertures: circular, annulus, circular with an opaque filament, knife-edge, and split-detector. Scale bar is 50 μm across.

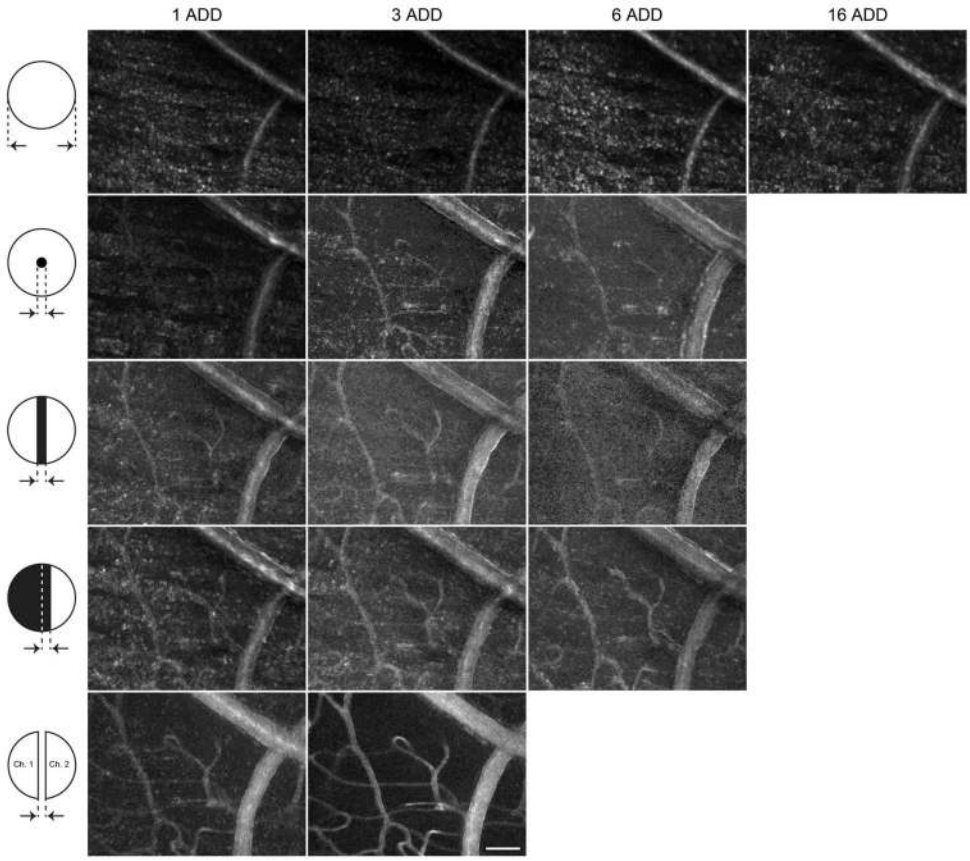

Fig. 6.

Perfusion maps corresponding to the image sequences averaged to create Fig. 5. Scale bar is 50 μm.

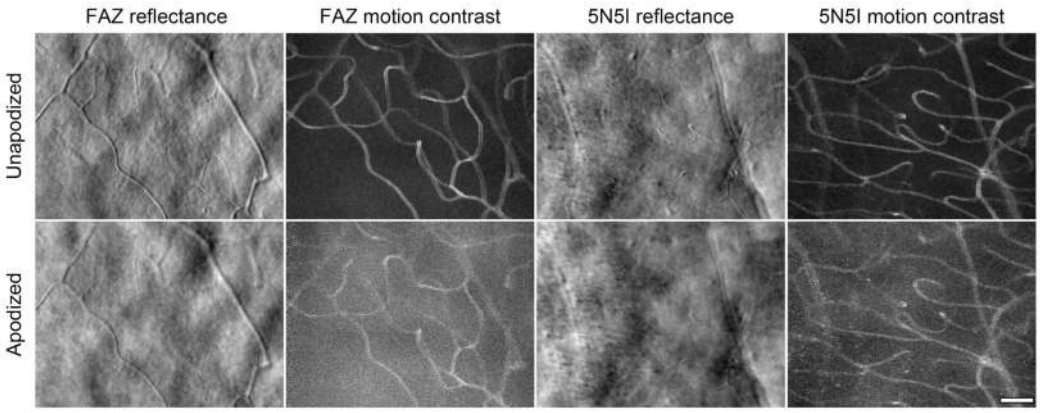

Fig. 7.

Split-detection AOSLO reflectance (first and third columns) and perfusion (second and fourth columns) images collected in subject AD_1025 with and without an apodized illumination pupil at the edge of the FAZ (0.6° temporal and inferior from fixation) and at 5° nasal and inferior from fixation (5N5I). Scale bar is 50 μm across.

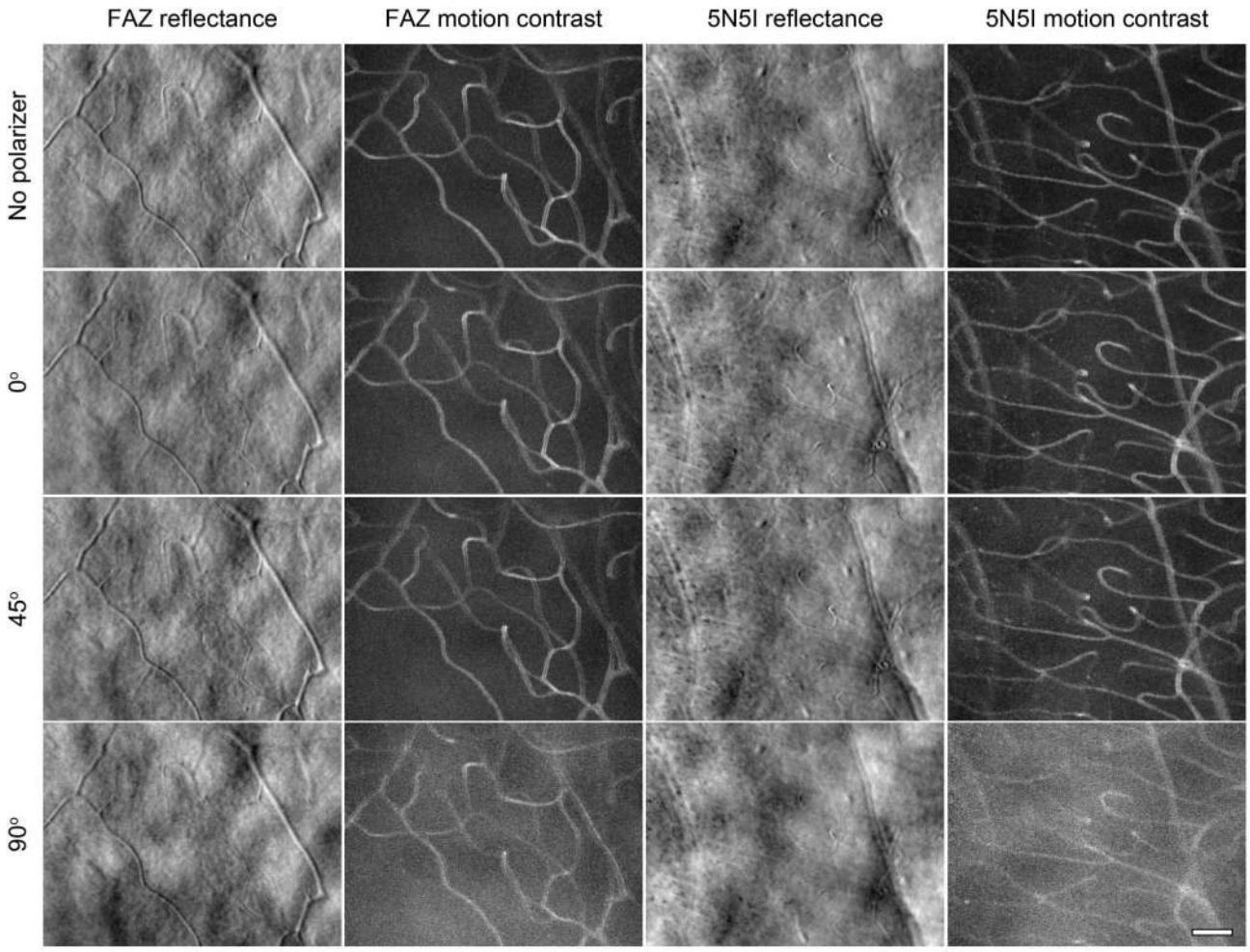

Fig. 8.

Split-detection AOSLO reflectance (first and third columns) and perfusion (second and fourth columns) from subject AD_1025 collected with linearly polarized illumination and a linear polarizer in different orientations in the exit pupil. The orientations indicated on the left are relative to the orientation for maximum transmission. Scale bar is 50 μm across.

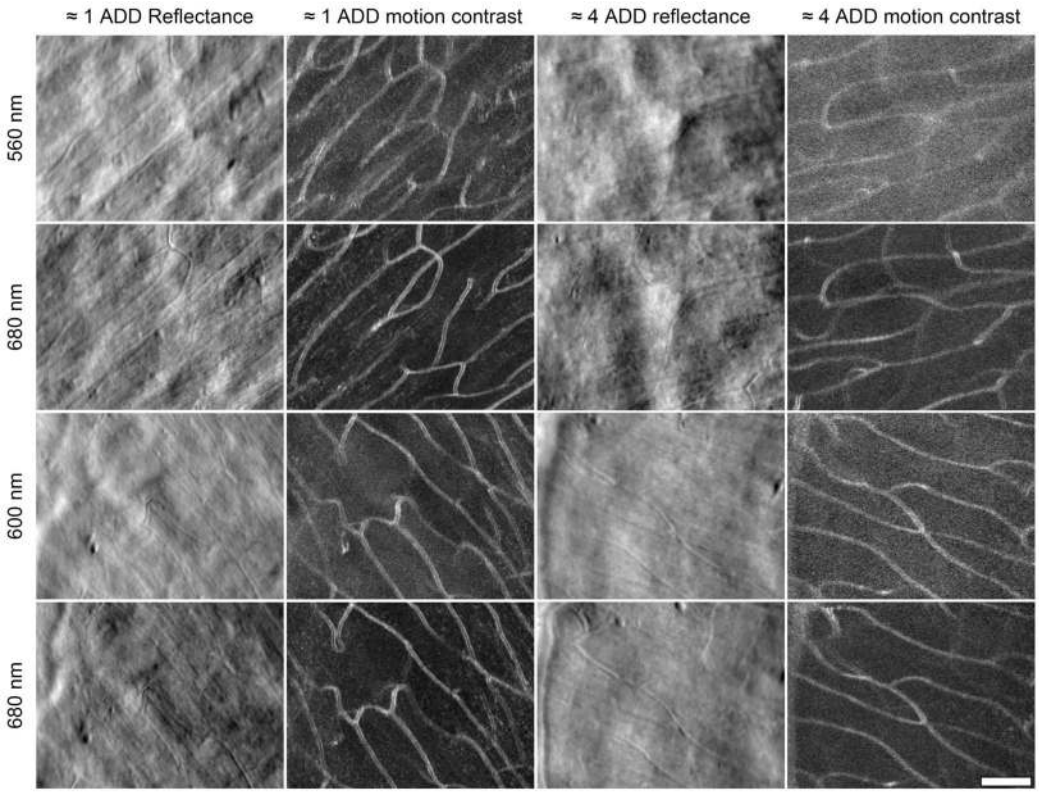

Fig. 9.

Split-detection AOSLO reflectance and perfusion images collected in subject JC_1246 using different wavelengths. Each retinal eccentricity imaged with 560 or 600 nm was re-imaged with 680 nm for comparison. The locations are as follows: 560 nm—12° nasal, 4° inferior (1 ADD) and 7° nasal, 4° inferior (4 ADD). 600 nm—13° nasal, 5° superior (1 ADD) and 7° nasal, 5° superior (4 ADD). All locations listed in degrees of visual angle relative to fixation. Scale bar is 50 μm across.

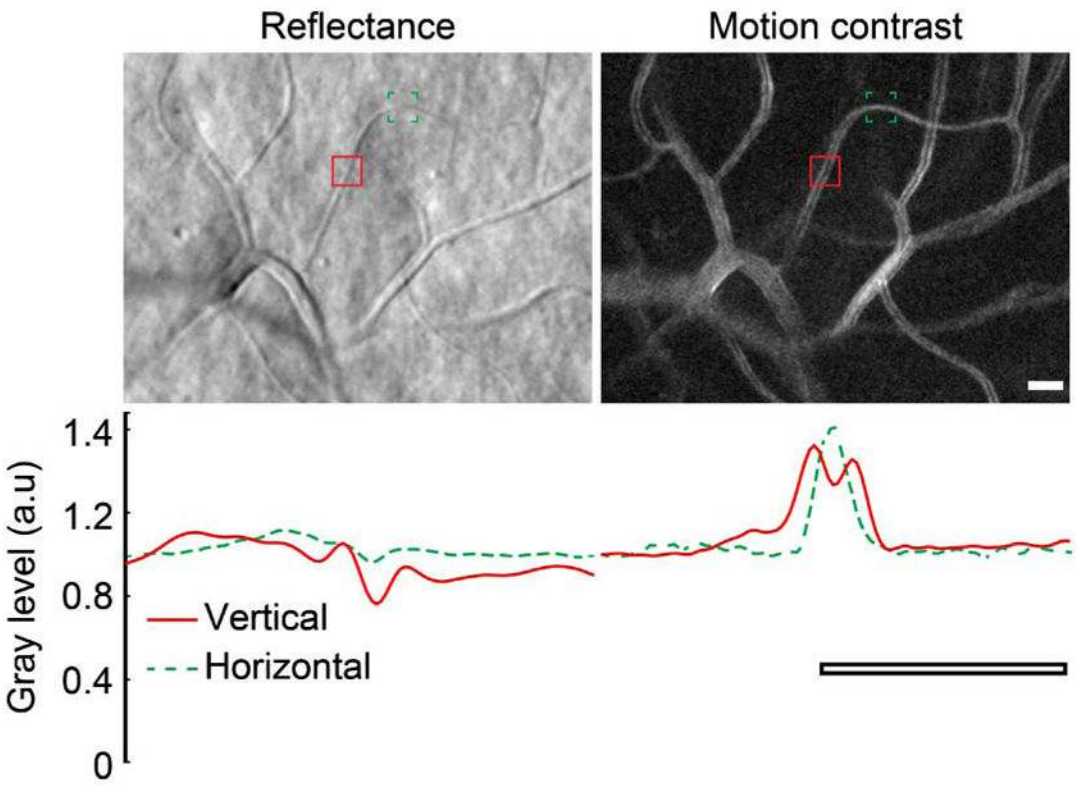

Fig. 10.

Split-detection motion contrast (perfusion) artifacts due to the asymmetric intensity profile of blood cells (bright on the left, dark on the right; Media 1). Top row: Split-detector reflectance and perfusion images collected in subject JC_0200 at 3° nasal to fixation. Bottom row: Cross sections through a single capillary at the points along its path boxed in the top row images. The vertical axis refers to gray levels in arbitrary units. Scale bars are 20 μm across.